Performance evaluation of a miniature laser ablation time-of-flight mass spectrometer designed for *in situ* investigations in planetary space research

A. Riedo,* A. Bieler, M. Neuland, M. Tulej and P. Wurz

Key performance features of a miniature laser ablation time-of-flight mass spectrometer designed for *in situ* investigations of the chemical composition of planetary surfaces are presented. This mass spectrometer is well suited for elemental and isotopic analysis of raw solid materials with high sensitivity and high spatial resolution. In this study, ultraviolet laser radiation with irradiances suitable for ablation (< 1 GW/cm^2) is used to achieve stable ion formation and low sample consumption. In comparison to our previous laser ablation studies at infrared wavelengths, several improvements to the experimental setup have been made, which allow accurate control over the experimental conditions and good reproducibility of measurements. Current performance evaluations indicate significant improvements to several instrumental figures of merit. Calibration of the mass scale is performed within a mass accuracy ($\Delta m/m$) in the range of 100 ppm, and a typical mass resolution ($m/\Delta m$) ~600 is achieved at the lead mass peaks. At lower laser irradiances, the mass resolution is better, about ($m/\Delta m$) ~900 for lead, and limited by the laser pulse duration of 3 ns. The effective dynamic range of the instrument was enhanced from about 6 decades determined in previous study up to more than 8 decades at present. Current studies show high sensitivity in detection of both metallic and non-metallic elements. Their abundance down to tens of ppb can be measured together with their isotopic patterns. Due to strict control of the experimental parameters, e.g. laser characteristics, ion-optical parameters and sample position, by computer control, measurements can be performed with high reproducibility. Copyright © 2012 John Wiley & Sons, Ltd.

Keywords: element analysis; isotope analysis; chemical composition; LIMS; space research; *in situ* measurement

Introduction

The chemical composition of planetary surfaces, their moons, asteroids and comets is of considerable interest for cosmochemistry and astrobiology.[1–3] The knowledge of the chemical composition, elemental and isotopic, puts constraints on models of the origin and evolution of our planetary system and extends our understanding of global scale processes shaping planetary surfaces, e.g. volcanic surface alteration, thermal heating effects, influence of space weathering effects, surface alteration by atmosphere or climate changes, etc. Isotopes of an element can be often used as powerful and robust tracers in the investigation of the origin and transformation of planetary matter.[2] They can yield information on early events occurring during the solar system formation because their abundances often are less disturbed than the elemental ones. A detailed analysis of isotopic patterns of radiogenic elements allows dating of planetary solids and measurements of isotopic patterns of bio-relevant elements, e.g. carbon, nitrogen, sulfur, etc., can be powerful indicators of past and present life in our solar system. All this information can be determined by *in situ* investigations of planetary materials using mass spectrometry.

So far, highly accurate and sensitive measurements for cosmochemistry could be only conducted by laboratory systems, using laser ablation inductively coupled mass spectrometry (LA ICP MS), thermal ionisation mass spectrometry (TIMS), glow discharge mass spectrometry (GDMS) and others. However, during the last

decade, considerable progress in developments of miniature mass analysers for space research was made.[4–11] At present, only a few well-established spectroscopic instruments are employed for chemical analysis of planetary surfaces from orbiting spacecraft, landers or rovers,[12] e.g. X-ray (XRS), Gamma-ray (GRS), neutron and alpha particle X-ray (APXS) techniques. Although the current spectroscopic instruments for space research have unquestionable achievements in the chemical investigation of planetary surfaces, these spectroscopic techniques are limited in terms of measurement sensitivity to the per mill level (only major and minor elements), and often only a restricted set of elements are amenable to the detection by these techniques.[13] Consequently, the uncertainties of modelling of chemical and mineralogical composition of the surfaces can be large due to only weak constraints given by the experimental results.[14] More sensitive instruments offering studies with high spatial resolution that would improve the chemical analysis of all elements are of considerable interest to the current space research.

Laser-induced breakdown spectroscopy (LIBS) and laser ionisation mass spectrometry (LIMS) are two new experimental

* Correspondence to: Andreas Riedo, Physics Institute, Universität Bern, Sidlerstrasse 5, 3012 Bern, Switzerland. E-mail: andreas.riedo@space.unibe.ch

Space Research and Planetary Sciences, Physics Institute, University of Bern, Sidlerstrasse 5 3012, Bern, Switzerland

techniques, which have been recently adopted for space research. Highly miniaturised instruments have been developed and have the capabilities to complement to the results obtained by other space spectroscopic instruments. A LIBS instrument is a part of the scientific payload of the Mars Science Laboratory (MSL) of NASA,[15,16] and LIMS (the LAZMA instrument) was a part of the scientific payload of the Phobos-Grunt lander and will be a part of the Luna-Glob lander, both by Roskosmos.[17–19] Unfortunately, the Phobos-Grunt mission was not successful due to technical problems of the rocket system dedicated for leaving low-earth orbit. Both, the LIBS and the LIMS instruments, have the potential to improve the *in situ* chemical analysis by means of increasing speed of the analysis and detection sensitivity of elements (isotopes). Although both instruments use pulsed laser sources, they differ significantly in the method of element detection and quantification.

The LIBS instrument uses the principles of optical spectroscopy for element identification and determination of elemental abundances. The instrument utilises spectral analysis of the light emitted from plasma plume generated by a focussed laser radiation on the solid sample. In the LIBS instrument on MSL, three spectrographs are used to disperse light in near-infrared, visible and UV spectral ranges. The elemental analysis is conducted by identifying the element-specific emission lines in the spectra. A full elemental analysis can be conducted only if the instrument can perform spectral analysis within 125 – 850 nm wavelength range with sufficiently high spectral resolution to resolve blended lines. The LIBS instrument does not require vacuum conditions and can be used to conduct the chemical analysis at distances of up to several meters from the objects of investigation. The advantages of LIBS instruments are the robust operation combined with simultaneous fast multi-element analysis, high lateral and vertical spatial resolution (depending on distance to the sample) and applicability under variable environmental conditions. However, the performance evaluations of LIBS instruments for space research show that the detection limits (DLs) of LIBS instruments for most elements lie in the ‰ to sub-per mill range. Furthermore, LIBS instruments often can support only a limited dynamic range of up to ~100 (due to background radiation) and exhibit a low detection efficiency for some of bio-relevant elements, such as carbon or sulfur (the important electronic transitions of these elements occur in far ultraviolet spectral range, outside the operational range of typical spectrographs).[20–28]

LIMS instruments utilise the mass spectrometric method for chemical analysis. Ions are generated during the ablation/ionisation process and are subsequently collected by a mass analyser enabling a mass separation and ion counting, thus direct elemental and isotopic analysis of the sample. This technique offers highly sensitive detection of almost all elements. Laboratory LIMS instruments have detection sensitivities down to ppb level for elemental and isotopic abundance measurements.[29] Although the laser ablation/laser ionisation source can be coupled with various mass analysers, a time-of-flight (TOF) mass analyser is best suited because of the pulsed nature of the laser system. TOF mass analysers allow for direct and fast analysis since a complete mass spectrum is recorded without any need for scanning. In addition, the TOF mass analyser can be highly miniaturised without compromising its performance compared to laboratory systems. The technical capabilities reported by various research groups showed that the miniature LIMS instruments can support highly sensitive measurements of elements (metals and non metals, such as C, Si, S, B and P) at abundances down to the ppm level.[10,11,27,28,30–33] Altogether, a miniature LIMS instrument

with small size, low weight and power consumption is well suited for sensitive and accurate *in situ* analysis on the chemical compositions of planetary surfaces in space research.[34] To date, several miniature LIMS systems, e.g. LAZMA,[4–6] LAMS,[7] LMS v1,[8] LMS v2,[9] LMS[10,11] have been developed for space research. They differ mostly in the method of confinement and detection of ions generated in the plasma plume.

During the last decade, we developed two miniature LIMS systems, LMS v1[8] and LMS v2,[9] which were designed for a lander and a rover, respectively. In this study, we report on further developments of LMS designed for a lander [10,11] and present the results on the key performance parameters such as mass calibration, mass resolution, dynamic range and achieved sensitivities.

Experimental

The details of the design and construction of LMS instrument can be found in previous publications.[8,10,11] The experimental setup utilised in this study is similar to that used earlier;[10] nevertheless, the instrument is now operated in new laboratory conditions and in a newly designed vacuum system. In comparison to the previous setup, several improvements to the optical alignment, front-end electronics and data acquisition system have been made. For example, a dedicated computer-controlled performance optimiser has been implemented to support reproducibility of sample preparation process and performance of mass analyser. These studies are performed using ultraviolet (UV) laser radiation ($\lambda = 266$ nm) for laser ablation/laser ionisation. As samples, we used different NIST standard reference materials (SRM). The technical design of the LMS instrument has not been changed so far and can be reviewed in detail in.[8,10,11]

Experimental setup and principle of operation

Figure 1 shows a current image of the laboratory system. The instrumental setup can be divided in three parts, (1) the computer control station, (2) electronics, e.g. power supplies, acquisition systems, vacuum system controls, etc., and (3) the instrumental setup itself with all the details shown in Fig. 2. The laboratory is environmentally controlled (temperature and humidity) and is kept at clean room conditions (Class 100). Thus, it provides the conditions for conducting highly clean chemical analysis, which are often required for the analysis of extra-terrestrial materials. A constant overpressure relative to the outside is kept to protect the laboratory from dust coming from outside. A laminar flow (ISO 2, class 100) is installed to protect the laser systems with their optics, the samples, vacuum chambers, etc., from possible dust and particles inside the laboratory. The temperature of the laboratory is kept at (22.0 ± 0.4) °C, and the humidity is controlled at (42.0 ± 0.5) °rel. humidity level. All parameters are monitored continuously and displayed in a web interface. Clean room conditions guarantee also stable operational conditions for all the instrumental equipment. Figure 2 displays the technical drawings of the current state of LMS system itself, the detailed overview of part (C) in Fig. 1. The experimental setup consists of two parts, (C1) the main UHV chamber (V1) with the laser system, optics and LMS instrument itself and (C2) the sample introduction/transport system in the smaller sized UHV chamber (V2). The base pressure in both UHV systems is typically in the low 10^{-8} mbar range, and is realised with turbomolecular pumps at each system and an additional ion getter pump for V1. The ion getter pump at V1 is only switched on if a pressure of 10^{-6} to 10^{-7} mbar is reached;

Figure 1. Overview of the instrument setup in the laboratory. (A) represents the remote control station; (B) the electronic equipment, e.g. measurement computer, power supplies, etc.; (C) the instrumental setup itself. Detailed information about part (C) can be found in Fig. 2. The argon sputter gun is not visible in this figure due to maintenance.
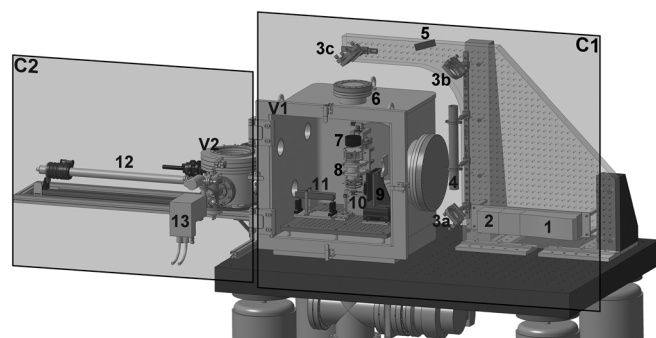

Figure 2. Technical drawing of the instrumental setup, detailed overview of part C in Fig. 1. The instrumentation can be divided in two parts, C1 and C2. C1: (1) laser system; (2) laser beam energy attenuator; (3a–c) laser beam deflection mirrors; (4) laser beam expander; (5) ultrafast photodiode; (6) entrance window into the vacuum chamber; (7) beam focusing lens; (8) mass analyser with detector; (9) x,y,z micro-translation stage; (10) sample holder with sample; (V1) main vacuum chamber. C2: (11 and 12) sample exchange and transport system; (13) argon sputter gun; (V2) vacuum chamber.

the turbomolecular pump of V1 is switched off and the gate valve between turbo pump and V1 is closed. This procedure ensures vibration-free conditions during measurement campaigns in V1. The UHV systems are separated with a computer controlled gate valve to prevent the two UHV systems from undesired exchange of gas from one system to the other. The gate valve will be only opened to exchange samples, introduced from V2 into V1.

An in-house designed sample provider is used to introduce new samples from V2 into the main V1 system without venting of the main chamber. With this procedure, more samples can be investigated in the mean time because V2 can be pumped down much faster than V1. An argon ion sputter gun (tectra GmbH, Physikalische Instrumente, Germany) is installed at V2 and is used to clean the sample surface from a possible surface contamination, if necessary. High purity argon gas is typically used for the cleaning process (Carbagas, Switzerland) although other gases, e.g. hydrogen, oxygen, nitrogen, etc., can also be used. The argon gun is typically operated at 3 keV, but ion beam energies can be tuned from

hundreds of eV to 5 keV. The angle of incidence of the incoming argon ions relative to the sample surface is ~10°; this angle can be, however, controlled by in-house designed ion deflection system.

The LMS mass analyser (8) is located within the UHV chamber V1. Samples are introduced with the sample transport system (11, 12) from V2 to V1 and positioned just below the entrance plate of the mass analyser, on a sample holder (10), which is attached to the x-y-z micro-translational stage (9). The accuracy of sample positioning and step resolution of these translational stages is ~2 μm. The distance between the sample surface and the entrance of the instrument is about 1 mm, and, if necessary, it is subsequently adjusted with the micro-translational stage. There is no contact between the sample surface and the entrance plate to avoid possible sample contamination. UV irradiation at 266 nm of a Q-switched Nd:YAG laser system (1) with a repetition rate of 20 Hz and pulse widths of $\tau \sim 3$ ns, measured at full width at half max (FWHM), is used to ablate and ionise surface material. The laser fluence can be remotely controlled by using a polarisation-sensitive beam attenuator which is installed in the laser system (2). The laser radiation is focused to a spot size of about $\varnothing$ 20 μm onto the sample surface by an optical system consisting of a beam expander (4) and a focussing lens (f/200, NA = 4), which is directly positioned above the ion mirror of the ion-optical system (7). The laser beam is guided via a dielectric mirror system (3a, 3b, 3c) and is aligned collinearly with the ion-optical axis of the TOF mass spectrometer. A small fraction of the laser fluence is reflected by the last dielectric mirror (3c) towards an ultrafast and high precision Si-photodetector (5) with rise and fall times of 40 ps and 50 ps, respectively (Alphalas GmbH, Germany) to record the laser fluence of each laser shot during a measurement campaign. The Si-photodetector signal is measured with an ADC card. The laser beam enters the TOF mass analyser (8) on the top of the ion mirror and travels along the ion-optical axis through the central hole ($\varnothing$ 6.4 mm) of the detector assembly, the ion-optical components, all way down until it reaches the sample surface (Fig. 3). The material ablated from the sample surface forms a hot plasma plume consisting of atomised and ionised species. Close proximity of plasma plume to the entrance of mass analyser allows collection of a major fraction of positive
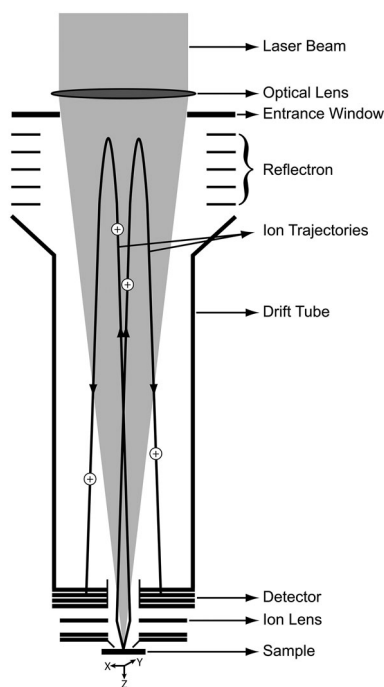
ω

Figure 3. Schematic drawing of LMS instrument, as shown in the overview of (8) in Fig. 2. The laser beam enters from the top and is focussed towards the sample surface after passing the TOF mass analyser, detector and ion-optical system. After the ablation/ionisation process, the ions are accelerated, focussed by the ion-optical lens system into the mass analyser and finally back reflected at reflectron system towards the ion detector.

Table 1. Overview of instrumental parameters of ion optics and laser system

LMS Ion Optics		
	Backplane	500 V
	Reflectron plate #5	−0 V
	Reflectron plate #4	−48. 8 V
	Reflectron plate #3	−50.0 V
	Reflectron plate #2	−14.6 V
	Reflectron plate #1	−19. 0 V
	Drift Tube	−662.6 V
	Ion Lens	−1568.6 V
	Snorkel	−499.5 V
	Ion Acceleration	−2487.6 V
Laser system	Nd:YAG system	
	Wavelength	266 nm
	Pulse duration	3.0 ns
	Repetition rate	20 Hz
	Spot size on sample	~20 μm
	Laser irradiances	< ~1GW/cm^2
Other	Focusing lens	f/200, NA = 4
	Sample distance to entrance of system	~1 mm
	Energy argon ions	Variable, typically 3 keV
	Incidence angle of argon ions	Typically 10°

ions to enter the mass analyser through the conical extraction electrode. After entering the interior of the mass analyser, ions are guided by electrical fields towards the detector. After initial acceleration, focussing and collimation by an electrostatic immersion lens, the ions fly through the field-free region (drift tube) and ion mirror (reflectron) where they are eventually reflected and guided towards the multichannel plate (MCP) detector. A pair of MCPs arranged in chevron configuration is used to generate the electric signal after the ions strike the MCPs. The ions arrive at the MCP detector in a sequence of times proportional to the square root of their mass-to-charge ratio (m/q). The electron current generated by the MCP plates is collected on four concentric anode rings and registered with two high speed ADC data acquisition cards, each with two channels. An overview of all the instrumental parameters, e.g. laser characteristics and ion optics, can be found in Table 1.

The trigger signal from the Q-switch of the laser system initiates the experimental cycle and triggers the data acquisition. Two high-speed ADC cards, one PCI (U1082A, AP240 with average firmware, Agilent) and one PCIe (U1084A, Agilent) card, are installed for data acquisition. Each card has two input channels with a vertical resolution of 8 bits for a single shot. The PCI card supports a sampling rate of 1 GS/s with an analogue bandwidth of 1 GHz for each channel whereas the PCIe allows a sampling rate of 2 GS/s with an analogue bandwidth of 1.5 GHz for each channel. For each card, these two channels can be combined into one channel with a doubled sampling rate of 2 GS/s and 4 GS/s, respectively. However, typically one channel of the PCI card is used to measure the signal from the ultrafast Si-photodetetctor and the other three channels to measure signals collected from three of the four anode rings.[8] The three inner anode rings are used for the measurements because of their high performance.[8] To protect the anode plate from possible charging effects, the fourth anode ring is short-circuited

with 50 Ω outside V1. With this measurement procedure, the ADC cards acquire in total $1.2 \cdot 10^5$ data points per laser shot or $2.4 \cdot 10^6$ data points/s, which are directly stored on the host computer. After accomplishment of the measurements, the data are subsequently forwarded from the host computer to a storage server. The TOF mass spectra are measured within a 20 μs time window defined by the acquisition card settings. This time window allows to measure mass spectra of elements within a mass range of ~600 amu/q.

Laser source characteristics

Figure 4 shows on the left and middle panel the plots of the measured UV laser beam profiles. Gaussian beam profiles and no hot spots are observed. Two iris diaphragms are used to select the most intense inner part (~∅ 1 mm) of the laser beam. The iris diaphragms are implemented between the parts 2 and 3a, and 3a and 4 (see Fig. 2). A microscopic image of a crater on an aluminium target is shown in the right panel in Fig. 4. The crater is circular and no extended rims are visible. The visible scratches and dots (white lines/dots) originate from the manufacturing process of the test aluminium sample and are not formed during the laser ablation.

Figure 5 shows the temporal laser pulse profile, measured by the Si-photodetector which was connected to one of the two channels of the ADC card. The pulse profile was determined by accumulation of 100 pulses and measured simultaneously during a mass spectrometric measurement campaign. The pulse width measured at FWHM of the laser pulse is about 3.0 ns. The stretched tail to the right side of the spectrum is characteristic response of the Si-photodetector.

Irradiance fluctuations

Figure 6 displays the shot-to-shot laser intensity fluctuations which were measured by a fast photodiode at three different laser irradiances (0.74 GW/cm^2, 0.57 GW/cm^2 and 0.33 GW/cm^2). Each data point in Fig. 6 (wave packet) corresponds to an average of
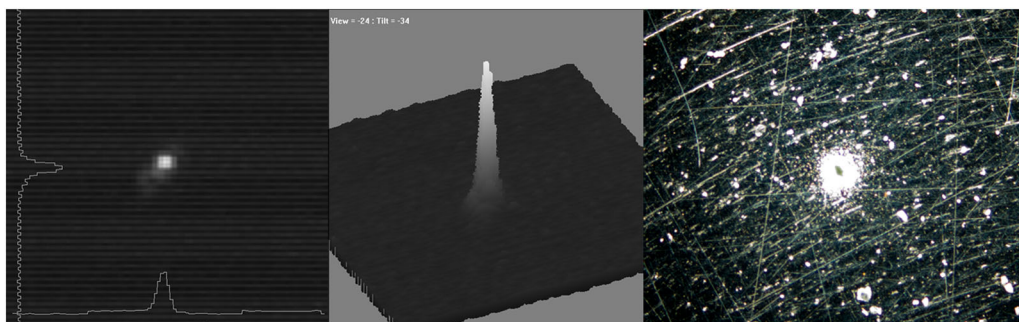
Figure 4. Left panel: plot of the UV beam intensity is shown. Beam profiles in both axis directions are Gaussian and are shown on the left and bottom side of the left panel plot. Middle panel: Same data are shown as in the left panel, but this time displayed in three dimensions. No hot spots are visible. The FWHM of the UV beam is in both axis directions about $\varnothing$ 20 μm. Right panel: Microscopic image of a crater on an aluminium target, which was generated during a test campaign.
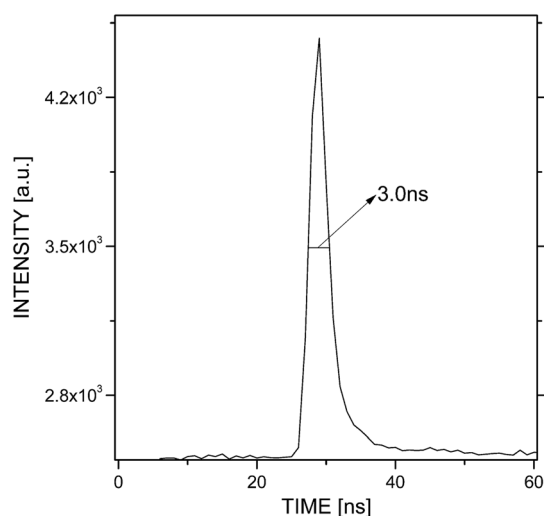

Figure 5. Typical pulse profile of the UV laser beam is shown. The profile consists of 100 averaged pulses and is measured with the ultrafast Si-photodetector connected to a channel of the PCI ADC card. The FWHM of the pulse is about 3.0 ns.

100 laser shots, and 300 such averages are displayed, corresponding to a total of 30 000 laser shots or to 25 min of laser activity at the 20 Hz repetition rate. The straight lines on the left side are linear regressions through the data and represent the temporal stability of the laser system. Although, on average, the laser system is stable with time (straight lines in the left panels), the relative differences of the individual points (100-shot averages) show intensity fluctuations of up to 40% at the lower laser irradiance of 0.33 GW/cm^2. By increasing the laser fluence the fluctuations decrease gradually but not significantly.

Shot-to-shot laser intensity fluctuations of Q-switched Nd:YAG laser systems are a common and well known problem. The laser irradiance fluctuations within the 0.1–1 GW/cm^2 can influence ion formation of different rates because the laser ablation/ionisation process is a highly non-linear process. Variation of ion yields at this laser conditions was reported from the other experiments.[35] Therefore, these laser intensity fluctuations have to be considered to conduct reproducible and quantitative measurements on the chemical compositions of sample surfaces. Single-shot measurements are not favoured for such laser intensity fluctuations, i.e. when using active Q-switched laser systems. Therefore, for the LMS system, we collect highly averaged spectra, histogramming of several thousands to hundred thousand, depending on the

analytical requirements of the measurement campaign. A single shot measurement can be considered if only qualitative information on the chemical composition of a sample is necessary.

Computer-controlled performance optimiser

The efficiency of computer-based optimisation of mass spectrometers with the adaptive particle swarm algorithm (APSA) has already been demonstrated by Bieler et al.[36,37] In this section, the implementation and principle of operation of APSA are discussed, new optimisation results of the LMS instrument are shown and more detailed description of the further developments of the LMS optimisation facility is given.

The Tool for Optimisation of Mass Spectrometers (TOM) uses a remotely controllable set of high voltage power supplies for automatic adjustment of voltages on the ion-optical system of mass analyser. By tuning the voltage settings, one can control the instrument performance in terms of mass resolution and/or ion transmission in flexible and reproducible way. APSA, which is introduced by Zhan et al. [38], is used as optimisation strategy. APSA is one of many derivatives of particle swarm algorithm originally introduced by Kennedy and Eberhart.[39,40] It belongs to the family of evolutionary algorithms. The algorithm is derivative free and can be applicable to a wide range of optimisation problems. It has been shown that APSA generally outperforms other popular optimisation algorithms. It is faster than the Nelder-Mead-Simplex for higher dimensional problems with dimensions higher than 4 and offers a faster convergence speed than genetic algorithms.[37]

The swarm in APSA consists of a defined number of particles (a set of instrument parameters) that evolve during an iterative process in order to increase their fitness. In terms of TOM one particle represents a set of voltages for the LMS instrument, and hence, a possible solution to the optimisation problem. Consequently, the swarm is the whole test set of solution candidates for one iteration. Because the optimisation problem is often multi-dimensional, more than only one best solution for the problem exists.[37]

Figure 7 shows an example of a particle swarm evolution during three iteration steps of an optimisation process. Each particle (circle) a, b and c of the swarm (swarm size = 3) represents a possible solution to the two-dimensional problem, numbers in the circle are indicating the current iteration. For the sake of simplicity of the example, the fitness function is only dependent on one parameter, hence defined as e.g. 1/|U| (the brighter, the better in Fig. 7). In every iteration, three different solutions are evaluated, their fitness compared and positions for the next iteration updated according to APSA search operations. More information about APSA can be found in.[39,40]
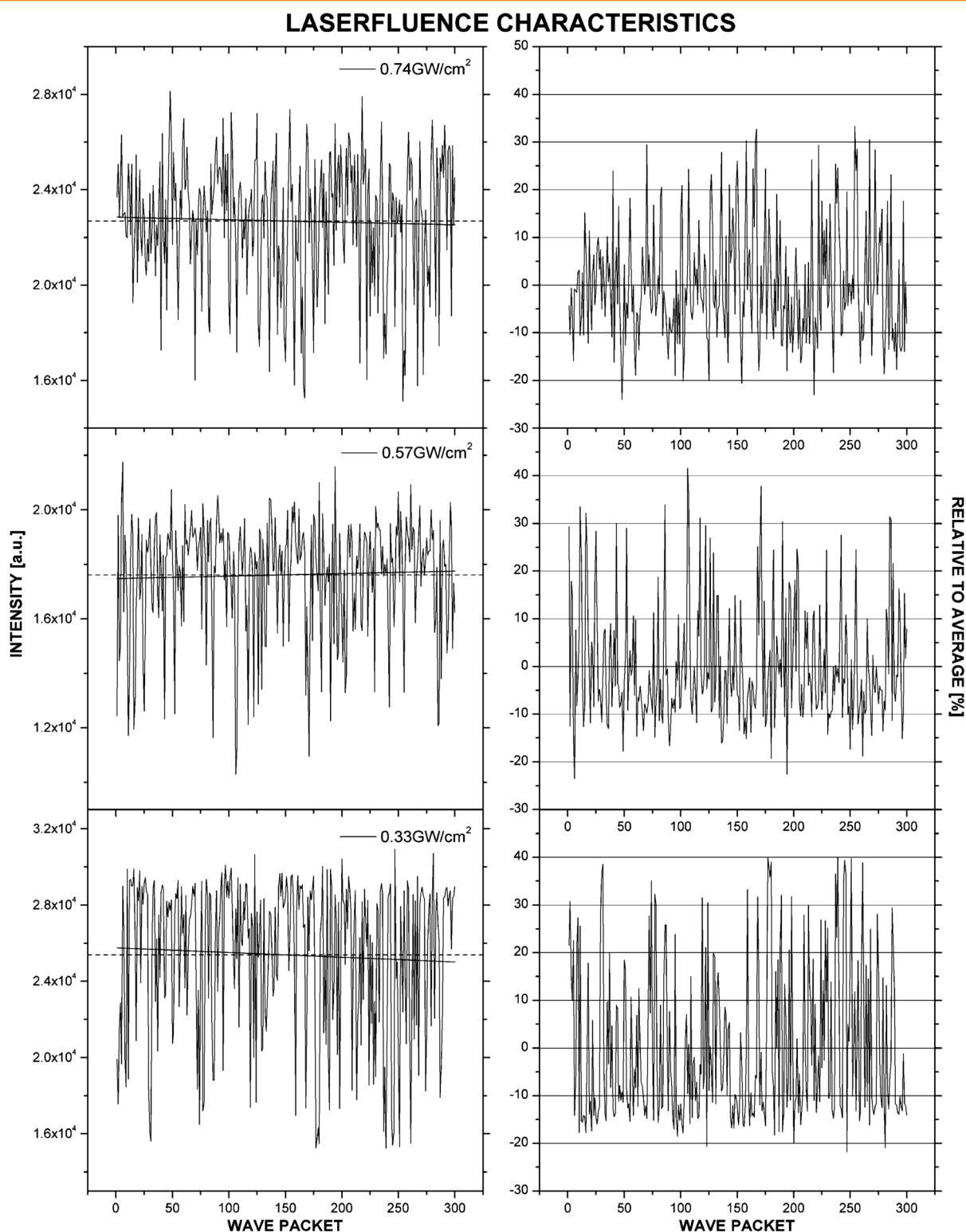
LASERFLUENCE CHARACTERISTICS

Figure 6. Left: Laser irradiance evolution of 30 000 (25 min, 20 Hz repetition rate) laser shots at three different laser irradiances (0.74 GW/cm^2, 0.57 GW/cm^2 and 0.33 GW/cm^2) is shown. Each data point (wave packet) corresponds to an accumulation of 100 laser shots; 300 wave packets are shown, corresponding to 30 000 laser shots. Dashed lines represent the average over all measured laser shots whereas the solid lines represent linear regressions through the data points. Right: Appropriate differences relative to the average of all measured laser shots. Irradiance fluctuations of several tens of % are clearly visible. The ultrafast Si-photodetector was used to measure the intensity of each laser pulse.

A functional block diagram of TOM (left) and the flow chart of the optimisation process (right) are shown in Fig. 8. The software is written in the Python programming language, which allows cross platform execution of the source code and provides libraries necessary to remotely control hardware devices either by RS-232 or TCP-IP.
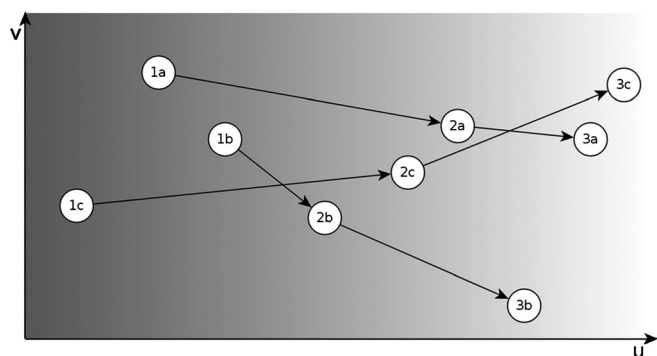
Figure 7. Example of a swarm evolution inside a two-dimensional search space with fitness only depending on one parameter U. The three particles building the swarm move from left to right and improve their fitness as the fitness function can be described as: the brighter, the better.

Using a graphical user interface, built with the Qt framework, the operator is allowed to define all parameters relevant for APSA, e.g. population size of the swarm, voltage limits for every electrode or the mathematical definition of fitness function. During optimisation, the interaction with the power supplies is realised via RS-232, where voltages are adjusted to evaluate the different solution candidates derived from APSA. The quality of each solution (its fitness) has then to be expressed as a single number through a user defined fitness function, e.g. $1/|U|$. Optimisation of an instrument is hence transformed into a problem of minimising that value.

The LMS system is operated at lowered detector gain (lower signal on anode rings) during optimisation to protect the ADC preamplifiers from possible high current signals coming from

particle solutions with high ion-optical transmission and mass resolution. Because measurement campaigns are finally conducted at highest possible detector gain (highest amplification of incoming ion signal), fitness functions which are weighted more on mass resolution than on an ion transmission are typically chosen, i.e. $-A/FWHM^2$ or $-A/FWHM^3$ where A corresponds to the amplitude and FWHM to the FWHM of the analysed mass peak.

Figure 9 shows the result of one optimisation run of the ^{56}Fe in NIST SRM 661 using APSA. The optimisation took about 45 min because of the slow internal power supply modules which set the voltages on ion optics. A swarm of six particles was defined by the user, and 300 spectra were accumulated for each particle in each step. The function $-A/FWHM^3$ was used as fitness function. The mass resolution of the ^{56}Fe line was successfully increased by a factor of about 6 compared to the non-optimised initial conditions (see Fig. 9), corresponding to an increase of mass resolution $m/\Delta m$ from 122 to 743 at increased sensitivity. However, not only the performance of ^{56}Fe was increased but also the performance of all other mass peaks is improved, e.g. detection efficiency of mass peak ^{54}Fe is clearly improved, and the mass lines of ^{55}Mn and ^{57}Fe became visible in the spectrum after optimisation.

Typically, several optimisation runs are necessary when starting with a completely detuned system. The reason is that the system depends not only on the applied voltages (ion optics, reflectron, etc.) but also on laser settings and distance between the sample surface and the ion-optical entrance of LMS. To date, the latter two parameters are not implemented into the optimisation loop and have to be still adjusted manually in between optimisation iterations. The lack of automation is not conceptual, as APSA does not distinguish between optimisation of voltages or any other parameter.[37,41]
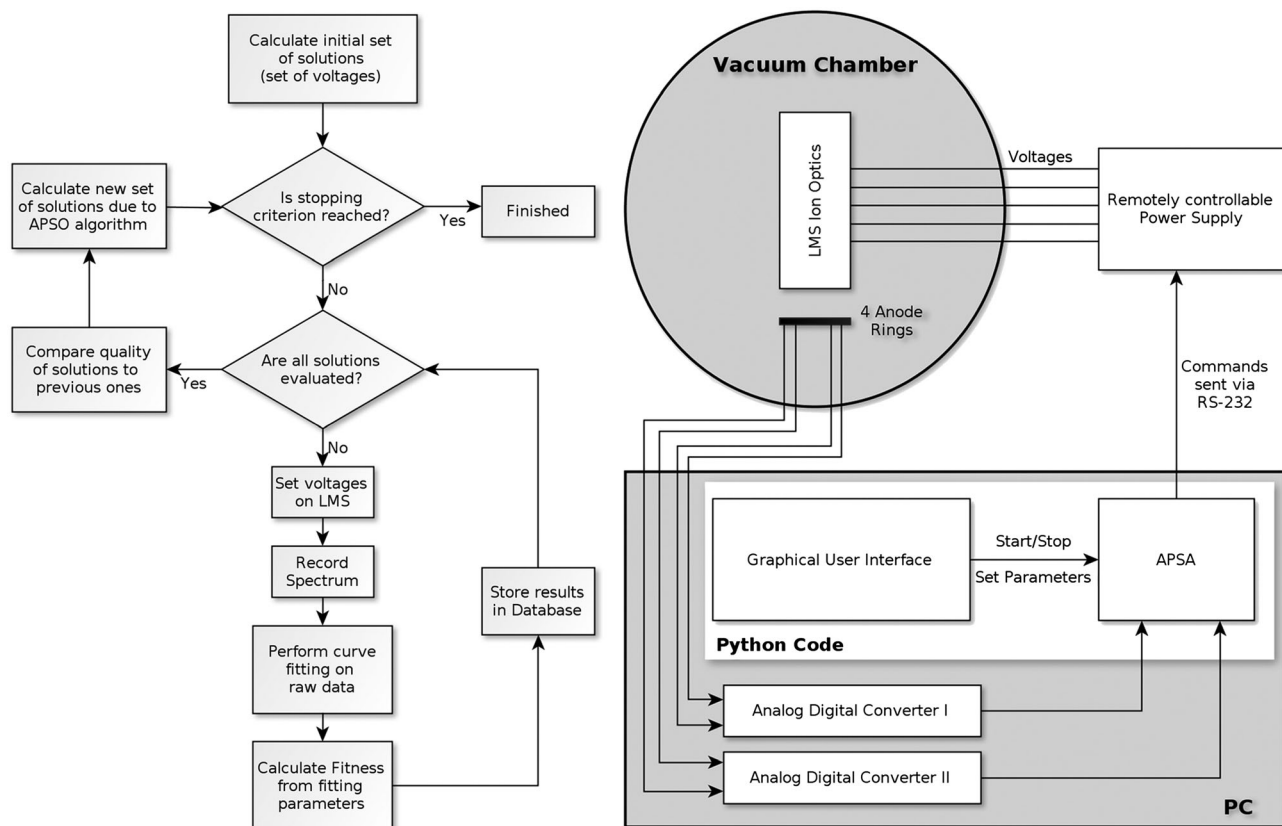

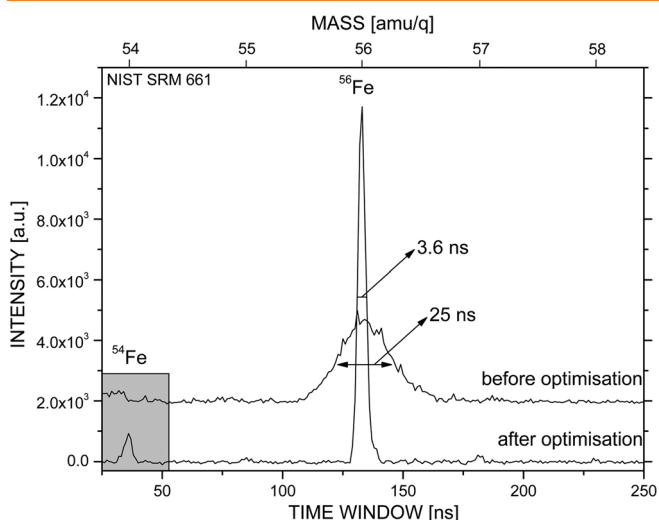**Figure 8.** Left: functional block diagram of the optimisation process. Right: schematic overview of the LMS TOM.

Figure 9. The section of mass a spectrum showing the ^{56}Fe peak in the NIST SRM 661 sample before and after the APSA optimisation procedure. The mass resolution was increased in one optimisation run by a factor of about 6, from m/Δm of 122 to 743. Not only the performance of ^{56}Fe was increased, but also ^{54}Fe is now clearly visible after optimisation. The time window centred to the time-of-flight of ^{56}Fe, the window is relative to the optimisation time window defined by the user.

But, even with these interruptions, APSA is sufficiently powerful to find its best solutions within the given settings/configuration. However, it is possible to prepare optimisation scans of the laser fluence with TOM and full implementation of these parameters in APSA is foreseen in the near future. For flight instrument, the laser fluence and the applied voltages of the system will be pre-optimised in prior laboratory calibration to avoid large optimisation campaigns during the mission. The distance between sample holder (sample wheel) and entrance to the instrument will be mechanically fixed at optimal position. In case of LMS on a rover the instrument has to be kept close to sample surface and optimised each time by APSA.

Flight instrument

Power consumption, weight and size of an instrument are optimised according to the requirements for the payload on the spacecraft, lander or rover. The LIMS system, LAZMA, which was implemented on the Phobos-Grunt lander, had volume of ~220 × 110 × 260 mm^3, weight of about 2.6 kg and required electrical power of 5 W.[4,42] Apart from the mechanical construction of the mass analyser itself, also the laser system, and electronics to supply the system and to control of the measuring cycle have to be miniaturised. In addition, if the ambient surface pressure is too high (>10^{-6} mbar), a miniature pumping system is required.

With current availability of light miniature laser systems, i.e. microchip lasers (weight of ~115 g, dimension of ~2.5 cm × 2.5 cm × 2.5 cm, power consumption <30 W), the laser mass spectrometer can be operated with a high repetition rate using passively Q-switched microchip lasers. These can be operated with a various pulse duration and wavelengths. Such lasers are available with high repetition rates of up to 10 kHz that will speed up measurements campaigns in space dramatically (for a 20 000 spectra campaign/laser shots ≙ 20 s). Also, if necessary, the re/optimisation process of the pre-optimised LMS instrument will be faster.[43] Although, the specified power consumption of <30 W is too high, in this case, for an implementation into a spacecraft directly, appropriate power buffering systems/hyper capacitors can be routinely implemented to support
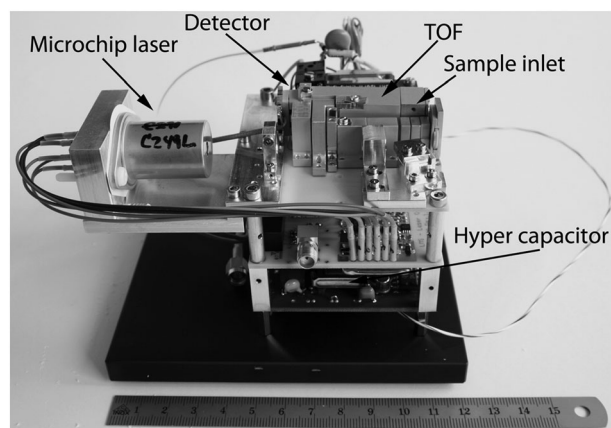

Figure 10. LMS v2 prototype instrument built onto a printed circuit board (top board), together with laser and temperature control board (middle board) and high-voltage supply board (bottom board). The sample inlet is a small hole on the centre of the entrance electrode (vertical plate at the right edge) of the TOF structure, which is on the top board. The micro-chip laser is on the left, with the laser optics on the right in the foreground of the top board. The scale of the shown rule in front of the prototype is in [cm].[9,34]

optimal power requirements.[44] Various microchip laser systems were already implemented in our prototype LIMS instruments, LMS v1 and LMS v2, designed in Bern for a Mercury lander and rover, which were part of the early concept of the BepiColombo mission.[45] Fig. 10 shows the LMS v2, prototype instrument designed for a rover.[34] More details on this system can be found in previous publications.[8,9,44]

If the ambient surface pressure on the investigated body is > 10^{-6} mbar, i.e. Mars with an ambient surface pressure of about 700 – 960 Pa, the instrument needs an additional vacuum system to protect the detector system (MCP detector) and a sample introduction system.[46] The ion-optical system can be built as vacuum enclosure at the same time, as it has been done for the RTOF instrument of the ROSINA experiment on the Rosetta mission,[47] which saves mass and complexity. Miniature turbo and drag pumps (dimensions of ~3 cm in diameter and ~8 cm length, power consumption 2 – 7 W, depending on the pressure, weight of ~150 g) are commercially available and used, i.e. on the MSL.[46,48] As a sample introduction system, a sample wheel, similar to that used for the Phobos-Grunt mission, can be implemented.[4]

A miniaturised signal acquisition card with interfaces (two channels à 2 GS/s sampling rate, 10 bit, power consumption of ~11.4 W) is available and designed in house, and is based on the design used for the Luna-Glob and Luna-Resurs mission.[49] In Table 2, an overview of the power consumption, weight and dimensions of all parts used for the functionality of the LMS system can be found. In comparison to the LAZMA space instrument,[4] the LMS instrument is in total about 500 g less heavy, has power consumption in the range of ~15 W and a volume of ~2600 cm^3. If the ambient surface pressure is in the range of 10^{-6} mbar or higher, the power consumption is increased by the consumption of an additional pump of about 9 W, and the weight is increased by ~150 g.

LMS instrumental performance and discussion

Mass spectrometric analysis and accuracy

The TOF mass spectra are measured on a linear time scale *t*. The transformation into mass scale is made with fixed scaling factors

Journal of
MASS SPECTROMETRY

Table 2. Overview of the power consumption, weight and dimensions of all parts used for the functionality of the LMS systems. The given numbers represent upper limits

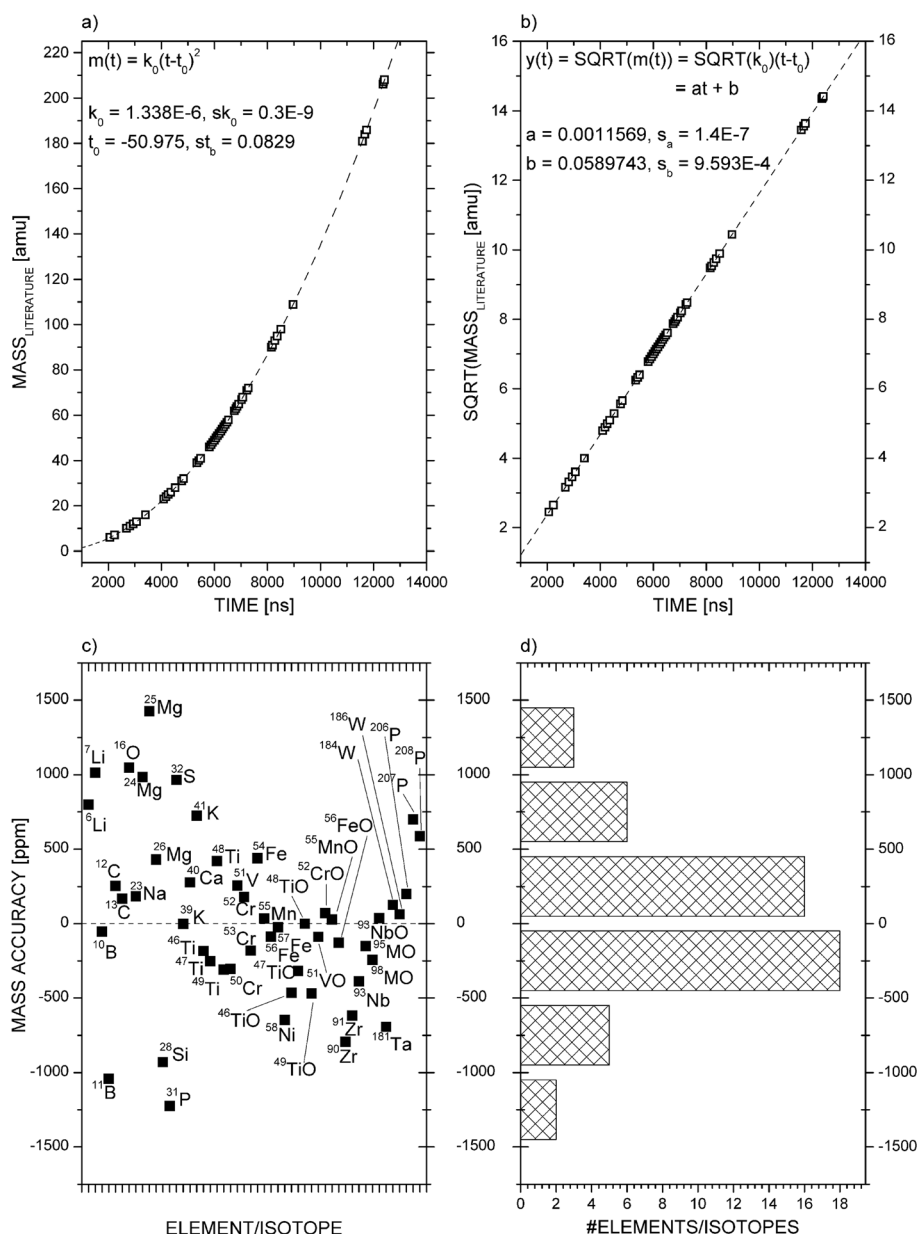|	Power consumption [W]	Weight [g]	Dimension [mm]
$<10^{-6}$ mbar			
Microchip laser	~2	~115	25 × 25 × 25 (h × w × d)
Acquisition card/Interfaces	11.4	~1400	180 × 240 × 60 (h × w × d)
LMS (Reflectron, Ion Optics, Detector)	1.9	~500	120 × 60 (h × diameter)
Total (with margin):	~15.3	~2015	~2615 cm³
$>10^{-6}$ mbar			
Pump	9	150	~80 × 30 (h × diameter)
Total (with margin):	< 24.3	~2165	~2618 cm³

Figure 11. Result of the mass calibration of the LMS system with its dedicated mass calibration software is shown. Up to 50 elemental isotopes and oxides of NIST SRM 664 were used to calibrate the TOF spectra into mass spectra. Panels a) and b) show the mass calibration curves with calibration constants and linear regression; c) mass accuracies defined as (measured - literature) over mass literature; d) corresponding histogram of mass accuracies. Up to 72% of the identified peaks have mass accuracies less than ± 500 ppm which is in good agreement with expectations on the instrumental performance (further details in text).

using the simple relation $m = k_0 (t–t_0)^2$, where m (amu) is the mass, t (ns) denotes TOF and k_0, t_0 are the calibration constants, which are determined experimentally.[10,11,47] Because the values of k_0 and, t_0 constants depend on the voltage settings of the reflectron and the other ion-optical components, they are subject to changes. The constants k_0 and, t_0 are calculated by using the parameters obtained by a linear regression of the flight times for elements and isotopes identified in the spectrum against the square root of the respective absolute mass from literature.

We designed a dedicated mass calibration software with a graphical user interface to convert TOF spectra directly into calibrated mass spectra. With the help of the graphical interface, the user can assign as many peaks in the TOF spectrum as can be assigned to an element or isotope or even to compounds, e.g. oxides, etc. A database with all the isotopic masses is present and used by the software for all the calculations. The centroid of the identified peak is calculated using a Gaussian fit, which is performed over a user-defined time window, typically, a FWHM of the peak with the peak maximum located in the centre.

Figure 11 shows the mass calibration of the instrument using the mass calibration software and the analysis of its accuracy. In this example, a NIST SRM 664 sample was investigated and up to 50 elements/isotopes and oxides in the mass range from [6]Li up to [208]Pb were used to convert the TOF spectrum into the mass spectrum. The chosen elements/isotopes have elemental/isotopic abundances in the %-range, i.e. [56]Fe with ~89% isotopic abundance, down to low ppm-range abundances, i.e. [207]Pb with ~53 ppm isotopic abundance.[10,50] Elemental abundance ratios are taken from the NIST data sheet, in % w/w, and isotopic ratios were calculated by assuming terrestrial isotopic ratios.[50] The constants for the mass scale calibration were calculated as $k_0 = (1.338E\text{-}6 \pm 0.3\ E\text{-}9)$ amu/ns^2 and $t_0 = (–50.975 \pm 0.0829)$ ns (panel a), the constants of the linear regression are $a = 0.0011569 \pm 1.4E\text{-}7$ and $b = 0.0589743 \pm 9.593E\text{-}4$ (panel b). In panel c, the mass accuracies defined as (measured – literature) over literature mass of the identified mass peaks are shown. A slight systematic shift from positive to negative deviations with increasing mass can be seen. This can be explained by the not uniform peak distribution over the investigated TOF range where a larger fraction of the identified peaks are localised at time of flights in the range of about 5 µs to 8 µs than outside, with the result that the linear regression has more weight in this range (panel c). Panel d shows the corresponding histogram of the mass error. The mass uncertainty is clearly Gaussian distributed with no significant tail in the positive or negative direction. Up to 72% of the mass uncertainties are located within the mass calibration accuracy of less than ± 500 ppm (panel d). This is in good agreement with the estimation that a system should have an accuracy of the mass calibration about ten times higher than the instrumental mass resolution. The LMS system has a mass resolution $m/\Delta m$ in the range of 500 to 1000 (depending on laser irradiance, see below), which corresponds to an expected accuracy of the mass scale in the range of about 100 ppm, as shown in panels d and c.

Mass resolution

Laser irradiances in the range of MW/cm^2 up to about 1GW/cm^2 were applied for ablation and ionisation of surface material. Because of its small size, the performance of the mass analyser is in first order limited by ion charge when an excessive amount of ions is generated during ablation process. Space charge effects, e.g. coulombic repulsion or sample charging, can cause a deterioration of the instrumental mass resolution.[10,11] However, also laser

pulse limitations and detector saturation effects can limit and reduce the mass resolution.

Figure 12 shows the mass resolution $m/\Delta m$ of the LMS system as function of mass for two different laser irradiances, i.e. in irradiance regimes below and above 100 MW/cm^2. In the laser irradiance regime of > 100 MW/cm^2, the typical mass resolution at Pb lies in the range of $m/\Delta m = 500$ to 600, which is sufficient to separate the Pb isotope peaks from each other.[10,11] In the lower laser irradiance regime, the mass resolution at Pb is larger by about 50% to $m/\Delta m \sim 900$ (Fig. 12). However, this improvement of mass resolution is correlated with decrease of detection sensitivity, and correlated to the ablation and ionisation efficiency of sample material at this laser irradiance regime. Figure 13 shows a high-resolution measurement of the lead isotopic pattern in the lead NIST SRM 981 reference sample. With the help of the computer-controlled performance optimiser, a mass resolution of up to $m/\Delta m \sim 850$ was reached. At this level, highly accurate measurements of the lead isotope composition at
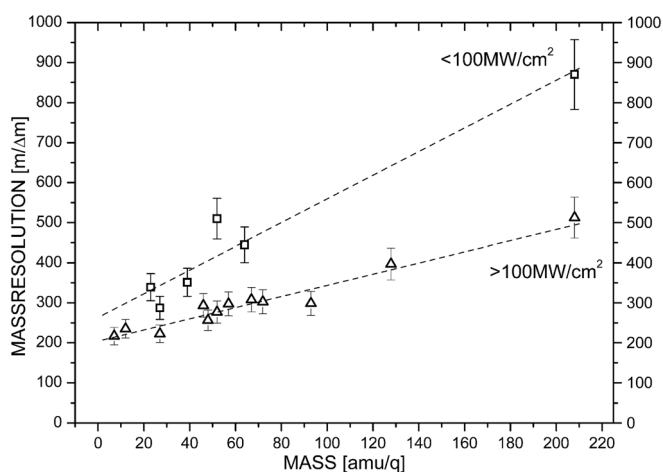

Figure 12. Instrumental mass resolution for two laser irradiance regimes, > 100 MW/cm^2 and < 100 MW/cm^2. At laser irradiances lower than 100 MW/cm^2, a mass resolution m/Δm of up to 900 at [208]Pb can be typically reached (Fig. 13) whereas at higher irradiances, the typical mass resolution at [208]Pb is in the range of 500 – 600.
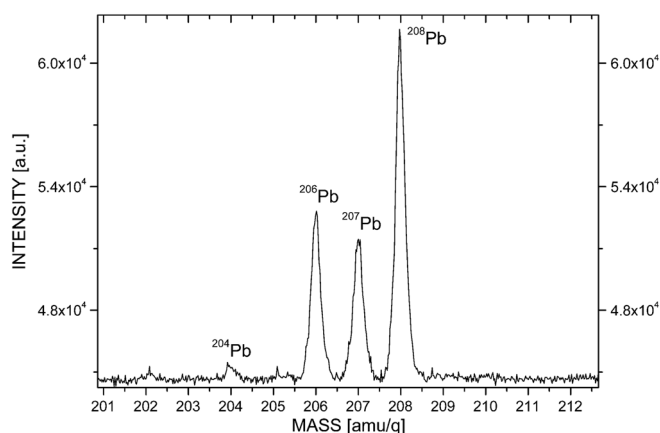

Figure 13. Section of mass spectrum of the lead isotopic pattern in the NIST SRM 981 standard sample is shown. The spectrum consists of 20 000 averaged laser shots/mass spectra. For [208]Pb, a mass resolution m/Δm of up to 850 is measured. At these conditions, high accurate isotopic analysis in the per mill and sub per mill accuracy range can be performed.

the per mill and sub per mill level can be performed. This accuracy opens possibility for the application of LMS to *in situ* dating of solids on planetary surfaces. Further details can be found in forthcoming publication.[51]

Dynamic range

Two high speed 8 bit ADC cards (PCI, PCI-E) with on-board averager firmware are used to measure signals collected on three of the four available anode rings. The averager firmware of the PCI card supports without memory overflow a maximum summation of 64 000 spectra, which corresponds to a maximum vertical resolution of 24 bit (64 000·8 bit) or to a maximum dynamic range of 7 decades per channel. The average firmware of the newer PCI-E ADC with extended memory supports a summation of up to 16.8 million, which corresponds to a maximum vertical resolution of up to 32 bit or to maximum dynamic range of up to 9 decades per channel. However, measurement campaigns are often performed with highly averaged spectra in the range of several 10 000 up to 100 000 averaged spectra, corresponding to about 6–7 decades of dynamic range/channel. To avoid possible memory

overflows on the PCI card spectra, packets of about hundred to several thousands of spectra are typically processed and averaged on board the ADC card and saved on the host computer.

The PCI-E shows, in comparison with the PCI, better performance regarding the internal card noise which for our purposes is the most important improvement of the acquisition system. The smallest signals will disappear in the noise if the internal noise of the card is too high. However, due to internal noise on each card, the effective dynamic range in each channel is lowered by about 1–2 decades to an effective and possible dynamic range of about 5–6 for each channel on both ADC cards.

To enhance the dynamic range of the LMS detection system (highest to the lowest detectable signal), the PCI and PCI-E channels are used at different gain levels. Based on the noise measurements of the data acquisition cards, measurement campaigns are typically conducted with PCI-E channels in the high (highest channel amplification, HG) and low (lowest channel amplification, LG) gain modes whereas one PCI channel is used in the middle gain mode (MG). To maintain measurement linearity, the amplitude range of all channels (HG, MG and LG) overlap at certain ranges with each other. Typically, LG channel is maintained at the gain, at which
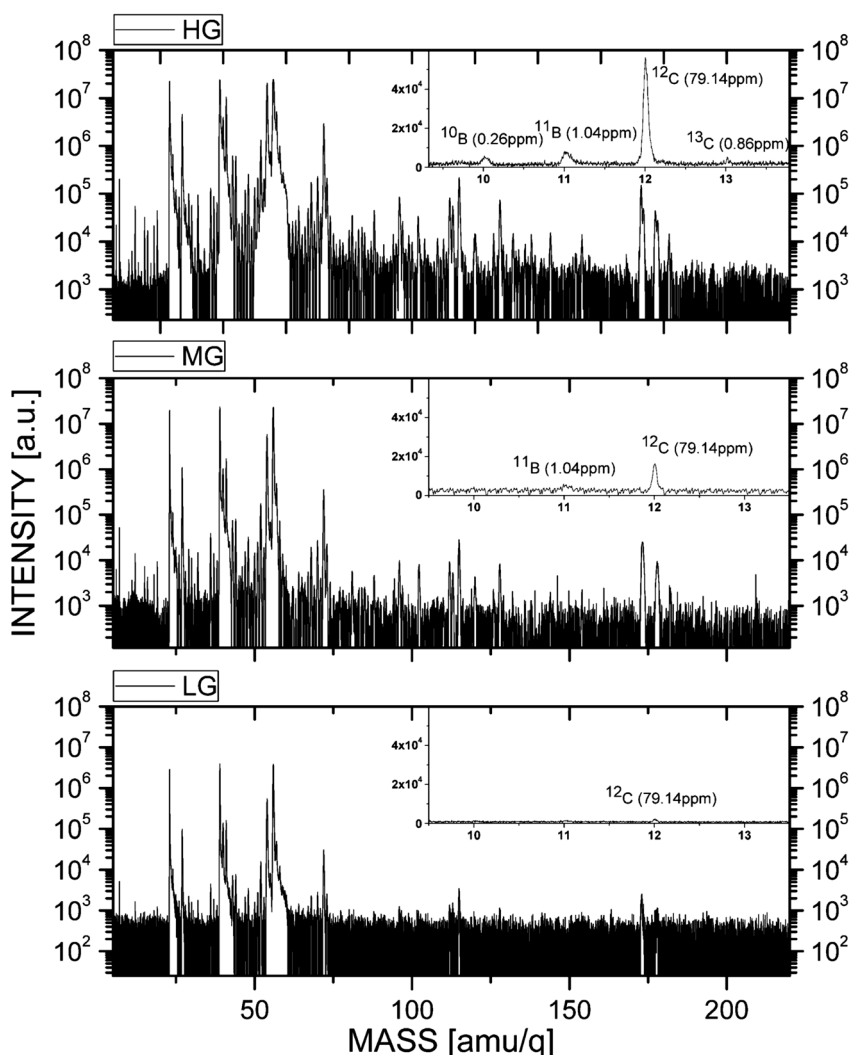

Figure 14. Typical measurement of NIST SRM 665 in the HG (top, PCI-E), MG (middle, PCI) and LG (bottom, PCI-E) channels is shown. The spectra consist of 100 000 averaged spectra and are displayed in logarithmic scale. The channel gains are increased stepwise by a factor of about ten from LG to HG. In each channel (HG, MG and LG), the background was subtracted for sake of clarity.

A. Riedo *et al.*

major elements can be measured without saturation effects of the card. In the HG channel, minor and trace elements can be measured with better vertical resolution but with saturation of mass peaks corresponding to major elements. MG is set between HG and LG and can be used for mass peaks which are already saturated in the HG channel but weakly detectable in LG, resulting in better vertical resolution and better measurement accuracy.

By combining LG and HG channels, the dynamic range can be increased by about 2 – 3 decades to an effective dynamic range of about 8 – 9. This is illustrated on the spectra obtained by measurements of NIST SRM 665 (Fig. 14, details below).

Figure 14 shows a standard measurement of NIST SRM 665 where a total of 100 000 spectra were averaged, and signals were recorded simultaneously in the LG (PCI-E), MG (PCI) and HG (PCI-E) channels. Hundred spectra are step wise averaged and saved on the host computer and subsequently averaged to obtain a statistically well averaged spectra (1000 à 100 average spectra). With this measurement procedure, it is possible to investigate the time evolution of averaged spectra, identify possible problems during campaign (e.g. a surface contamination), or a chemical inhomogeneity with depth.[11] The channel gains were increased step wise by factor of ten from LG to HG to enhance the dynamic range of the detection system. For the reference, elemental abundances in the sample are measured by NIST and given in % w/w; expected isotopic abundances were calculated by assuming terrestrial isotopic abundances.[50] In the LG spectra (bottom panel of Fig. 14), major and minor elements/isotopes with elemental/isotopic abundances down to ~100 ppm are clearly visible. ^{12}C at a total abundance of about 79 ppm is easily detected (see insert in Fig. 14, bottom panel). By increasing the channel gain by a factor of ten (MG), already elements and isotopes down to ~1 ppm can be observed, e.g. ^{11}B with a total abundance of this isotope of about 1 ppm (see insert in Fig. 14, middle panel). By further increase of the channel gain by a factor of ten (the HG channel), the sensitivity is maximised (see top panel of Fig. 14) where elements and isotopes with abundances below the ppm range, e.g. ^{10}B and ^{13}C with respective abundances of 0.26 ppm and 0.86 ppm, are now clearly detectable. In the HG spectra, major and minor elements and their isotopes with abundances down to the %-level are saturated and have to be analysed in the MG or LG channel.
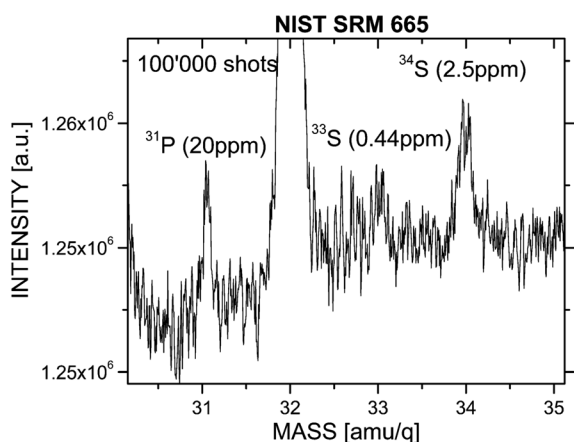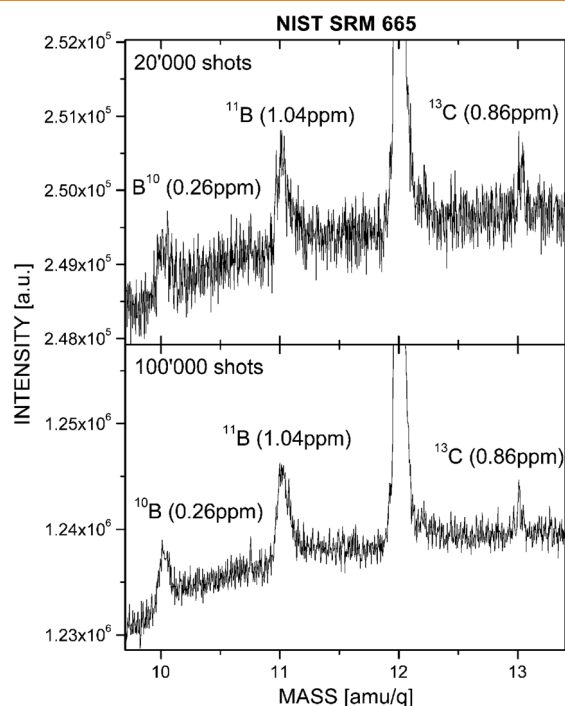

Figure 16. Sections of HG spectra of NIST SRM 665 in the mass range of boron and carbon after 20 000 (top, sub-set of 100 000 averaged spectra) and 100 000 (bottom) averaged spectra/laser shots in linear scale are shown. The displayed data are equal to the data shown in Fig. 14. Already after 20 000 averaged spectra (top) peaks down to sub ppm level are clearly detectable, e.g. ^{10}B or ^{13}C with abundances of about 0.26 ppm and 0.86 ppm, respectively. By increasing the number of averages to 100 000, the SNR can be improved by a factor of about 2 to 3 (bottom panel).

Detection sensitivity and DLs

The result of all system improvements, e.g., computer-controlled performance optimiser, better performance on electronic acquisition systems, UV irradiation, etc., with respect to the previous version[10,11] can be fully appreciated in Figs 15–17, which show sections of mass spectra in the HG channel of NIST SRM 665 at different mass ranges. The presented data are equal to the data

Figure 15. Section of HG spectrum of NIST SRM 665 in the mass range of phosphorus and sulfur after 100 000 averaged spectra/laser shots in linear scale is shown. The presented data are the same as the data shown in Fig. 14. Phosphorus and all sulfur isotopes, even ^{33}S with a total abundance of about 0.44 ppm, can be clearly detected.
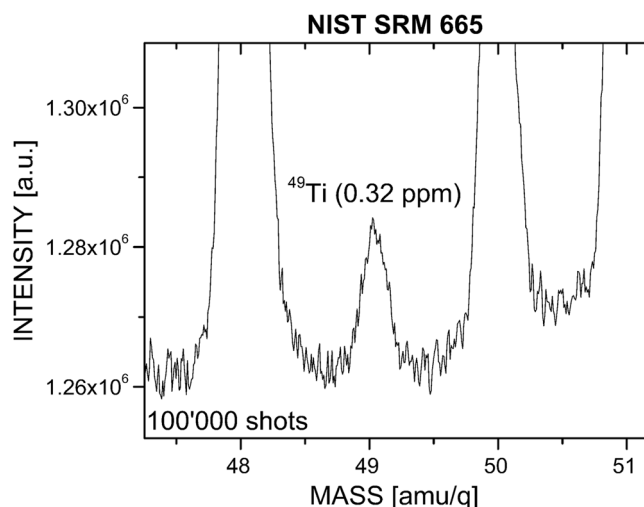

Figure 17. A section of HG spectrum of NIST SRM 665 displays ^{49}Ti mass peak measured after accumulation of 100 000 single laser shot spectra. ^{49}Ti with total abundance of this isotope of about 0.32 ppm can be easily observed.

Table 3. Elemental abundance ratios for different metallic and non-metallic elements as given by NIST for SRM 665 and SRM 661 (second column). The ratios are given in weight fractions [ppm]. Isotopic ratios were calculated by using terrestrial isotopic ratios,[50] in weight fractions [ppm] (third column). Elemental and isotopic abundances calculated for laser ablation mass spectrometry are given in fourth and fifth columns, in atom fractions [ppm]. SNR and calculated DL (atomic fraction) for each isotope are given in the last two columns

Element	Weight fraction element [ppm]	Weight fraction isotope [ppm]	Atom fraction element [ppm]	Atom fraction isotope [ppm]	SNR	Detection limit [ppb]
B (SRM 665)	1.3	^{10}B: 0.26	6.7	^{10}B: 1.34	6	220
		^{11}B: 1.04		^{11}B: 5.38	9	600
C (SRM 665)	80.0	^{12}C: 79.14	371.8	^{12}C: 367.84	79	4660
		^{13}C: 0.86		^{13}C: 3.98	1	3980
P (SRM 665)	20.0	^{31}P: 20.0	36.0	^{31}P: 36.05	7	5150
S (SRM 665)	59.0	^{32}S: 56.04	102.7	^{32}S: 97.57	135	720
		^{33}S: 0.44		^{33}S: 0.77	1	770
		^{34}S: 2.51		^{34}S: 4.37	7	620
Ti (SRM 665)	6.0	^{46}Ti: 0.50	7.0	^{46}Ti: 0.58	56	10
		^{48}Ti: 4.42		^{48}Ti: 5.16	378	10
		^{49}Ti: 0.32		^{49}Ti: 0.38	31	10
V (SRM 665)	6.0	^{51}V: 5.99	6.6	^{51}V: 6.56	290	20
Cr (SRM 665)	70.0	^{52}Cr: 58.65	75.2	^{52}Cr: 62.97	1885	30
		^{53}Cr: 6.65		^{53}Cr: 7.14	221	30
Mn (SRM 665)	57.0	^{55}Mn: 57.0	57.9	^{55}Mn: 57.9	648	90
Zr (SRM 661)	90.0	^{90}Zr: 46.31	54.2	^{90}Zr: 27.91	246	110
		^{91}Zr: 10.10		^{91}Zr: 6.09	80	80
Nb (SRM 661)	220.0	^{93}Nb: 220.0	130.2	^{93}Nb: 130.2	1047	120

shown in Fig. 14, but this time displayed in linear scale. To show the performance of the system, the highly intense mass peak of ^{32}S with isotopic abundance of ~56 ppm in Fig. 15 and mass peak ^{12}C in Fig. 16 with isotopic abundance of ~79 ppm are not fully shown. Signal-to-noise ratio (SNR) is defined as the ratio between the integrated peak area and the noise area, calculated as the standard deviation of a noise (measured outside the spectral range where no mass peak is detected) times the width of analysed elemental/isotopic peak.

Figure 15 shows the section of the HG spectrum in the mass range of the non-metallic elements phosphorus and sulfur in a spectrum of 100 000 averages. Phosphorus with elemental abundance of about 20 ppm and all sulfur isotopes, even ^{33}S with total abundance of about 0.44 ppm, can be clearly identified, which was not possible with earlier LMS setups.[10,11]

Top panel of Fig. 16 shows a section of the HG spectrum in the mass range of boron to carbon after 20 000 (top panel, sub-set of 100 000 averaged spectra) and 100 000 (bottom panel) averaged spectra/laser shots, respectively. Already after 20 000 averaged spectra/laser shots elements/isotopes in the sub ppm level, e.g. ^{10}B and ^{13}C with abundances of about 0.26 ppm and 0.86 ppm, respectively, can be clearly detected. By averaging over 100 000 spectra, the SNR is improved by a factor of about 2 to 3, as shown in the bottom panel of Fig. 16. In Fig. 17, ^{49}Ti with total abundance of this isotope of ~0.32 ppm and SNR of about 31 can be clearly observed.

For quantifying the DL, the SNR has to be taken into account. The DL can be calculated as measured elemental/isotopic abundance over SNR, whereas the abundance corresponds to the atom fraction abundances. For comparison with our mass spectrometric results, the abundances of elements quoted by NIST as weight fractions have to be transformed into atomic fraction abundances. In Table 3, NIST quoted elemental weight fractions and transformed atomic fractional abundances of different metallic and non-metallic elements in SRM 665 and SRM 661

are given. Isotopic abundances were calculated by assuming terrestrial isotopic ratios given in.[51] ^{32}S with total abundance of ~56 ppm and SNR of 135 is easily detectable whereas ^{33}S with total abundance of ~0.44 ppm and just visible above the noise (Fig. 15) shows the DL range for non-metallic elements/isotopes: few hundredths of ppb for non-metallic elements/isotopes. By using the isotopic abundance of 97.6 ppm (atom fraction, Table 3) and SNR of 135 of the detected ^{32}S peak one gets a DL of 720 ppb (atom fraction), which fully agrees with the measured abundance of the ^{33}S isotope with abundance of 770 ppb (atom fraction, Table 3), 440 ppb (weight fraction, Table 3), respectively. To quantify the DL for metallic elements/isotopes ^{49}Ti with a total abundance of 380 ppb (atom fraction, Table 3) and SNR of 31 can be used (Fig. 17). In this case a DL of about 10 ppb (atom fraction) can be calculated, which corresponds to DL of < 20 ppb in weight fraction for titanium (Table 3). In addition, different other metallic elements/isotopes, i.e. V, Cr, etc., show similar DLs in the range of tens of ppb (Table 3). Hence, the presented results and calculations clearly show that measurements with the LMS system on non-metallic and metallic elements and their isotopes with abundances of hundredths and tens of ppb, respectively, can be accomplished.

Conclusion

Owing to improvements made to the detection and acquisition system including implementation of a new and more sensitive data acquisition system, a computer-controlled performance optimiser, and dedicated analysis software, the performance of the LMS instrument could be improved significantly. The presently achievable effective dynamic range of the instrument allows mass spectrometric analysis within at least eight orders of magnitude. The measurement sensitivity derived from the analysis of the NIST SRM has been improved by almost two orders of magnitude. Non-metallic and metallic elements and

their isotopes with abundances down to hundredths and even tens of ppb, respectively, can be detected with the LMS instrument. With a mass resolution $m/\Delta m$ of almost 1000 at Pb and mass accuracy $\Delta m/m$ in the range of 100 ppm, the system has the potential for highly accurate and sensitive *in situ* measurements of the chemical composition of planetary materials. Each system parameter, e.g. voltages of the ion-optical system, laser fluence, sample position, etc., can be controlled on a reproducible way by custom-written software running on a regular lab computer. This allows choosing the optimal conditions for investigations of specific problems but also guarantees highest possible reproducibility of measurements from the instrumental point of view. Although, a high instrumental performance has been achieved, so far, further improvements are anticipated by implementation of more sensitive detection and acquisition systems as well as short pulse duration laser sources. The improved miniaturised LMS system with its enhanced performance represents a powerful instrument for *in situ* investigations of the chemical compositions of planetary materials.

Acknowledgements

References

[1] J. Chela-Flores, N. Kumar. Returning to Europa: can traces of surficial life be detected? *Int. J. Astrobiol.* **2008**, 7, 263–269.

[2] H. Y. McSween, G. Huss. *Cosmochemistry*. Cambridge University Press: Cambridge, **2010**.

[3] I. N. Tolstikhin, and J. D. Kramers. *The evolution of matter*. Cambridge University Press: Cambridge, **2008**.

[4] G. G. Managadze, P. Wurz, R. Z. Sagdeev, A. E. Chumikov, M. Tuley, M. Yakovleva, N. G. Managadze, A. L. Bondarenko. Study of main geochemical characteristics of Phobo's regolith using LMS time-of-flight mass spectrometry. *Sol. Sys. Res.* **2010**, 44, 376–384.

[5] L. M. Zelenyi, A. V. Zakharov. Phobos-Grunt project: Devices for scientific studies. *Solar Syst. Res.* **2010**, 44, 359–361.

[6] L. M. Zelenyi, A. V. Zakharov, G. M. Polischuk, M. B. Martynov. Project of the mission to Phobos. *Solar Syst. Res.* **2010**, 44, 15–25.

[7] W. B. Brinckerhoff, G. G. Managadze, R. W. McEntire, A. F. Cheng, W. J. Green. Laser time-of-flight mass spectrometry for space. *Rev. Sci. Instrum.* **2000**, 71, 2159–2164.

[8] U. Rohner, J. A. Whitby, P. Wurz. A miniature laser ablation time-of-flight mass spectrometer for in situ planetary exploration. *Meas. Sci. Technol.* **2003**, 14, 2159–2164.

[9] U. Rohner, J. Whitby, P. Wurz, S. Barabash. A highly miniaturised laser ablation time-of-flight mass spectrometr for planetary rover. *Rev. Sci. Instrum.* **2004**, 75, 1314–1322.

[10] M. Tulej, M. Iakovleva, I. Leya, P. Wurz. A miniature mass analyser for in-situ elemental analysis of planetary material–performance studies. *Anal. Bioanal. Chem.* **2011**, 399, 2185–2200.

[11] M. Tulej, A. Riedo, M. Iakovleva, P. Wurz. On applicability of a miniaturised laser ablation time of flight mass spectrometer for trace elements measurements. *Int. J. Spec.* **2012**, 2012, Article ID 234949.

[12] H. Y. McSween Jr., I. O. McGlynn, A. D. Rogers. Determining the modal mineralogy of Martian soils. *J. Geophys. Res.* **2010**, 115, E00F12.

[13] M. Tulej, A. Riedo, M. Neuland, M. Iakovleva, P. Wurz. Elemental and isotopic in situ analysis in space research. *GI* **2012**, submitted.

[14] P. Wurz, J. A. Whitby, U. Rohner, J. A. Martin-Fernandez, H. Lammer, C. Kolb. Self-consistent modelling of Mercury's exosphere by sputtering, micro-meteorite impact and photon-stimulated desorption. *Planet. Space Sci.* **2010**, 58, 1599–1616; *Corrigendum Planet. Space Sci.* **2010**, 58, p. 2051.

[15] S. Maurice, R. C. Wiens, M. Saccoccio, B. Barraclough, O. Gasnault, O. Forni, N. Mangold, D. Baratoux, S. Bender, G. Berger, J. Bernardin, M. Berthé, N. Bridges, D. Blaney, M. Bouyé, P. Caïs, B. Clark, S. Clegg, A. Cousin, D. Cremers, A. Cros, L. DeFlores, C. Derycke, B. Dingler, G. Dromart, B. Dubois, M. Dupieux, E. Durand, L. d'Uston, C. Fabre, B. Faure, A. Gaboriaud, T. Gharsa, K. Herkenhoff, E. Kan, L. Kirkland, D. Kouach, J.-L. Lacour, Y. Langevin, J. Lasue, S. Le Mouélic, M. Lescure, E. Lewis, D. Limonadi, G. Manes, P. Mauchien, C. McKay, P.-Y. Meslin, Y. Michel, E. Miller, H. E. Newsom, G. Orttner, A. Paillet, L. Parès, Y. Parot, R. Pérez, P. Pinet, F. Poitrasson, B. Quertier, B. Sallé, C. Sotin, V. Sautter, H. Séran, J. J. Simmonds, J.-B. Sirven, R. Stiglich, N. Striebig, J.-J. Thocaven, M. J. Toplis, D. Vaniman. The ChemCam Instrument Suite on the Mars Science Laboratory (MSL) Rover: Science Objectives and Mast Unit Description. *Space Sci. Rev.* **2012**. DOI 10.1007/s11214-012-9912-2

[16] R. C. Wiens, S. Maurice, B. Barraclough, M. Saccoccio, W. C. Barkley, J. F. Bell III, S. Bender, J. Bernardin, D. Blaney, J. Blank, M. Bouyé, N. Bridges, N. Bultman, P. Caïs, R. C. Clanton, B. Clark, S. Clegg, A. Cousin, D. Cremers, A. Cros, L. DeFlores, D. Delapp, R. Dingler, C. D'Uston, M. D. Dyar, T. Elliott, D. Enemark, C. Fabre, M. Flores, O. Forni, O. Gasnault, T. Hale, C. Hays, K. Herkenhoff, E. Kan, L. Kirkland, D. Kouach, D. Landis, Y. Langevin, N. Lanza, F. LaRocca, J. Lasue, J. Latino, D. Limonadi, C. Lindensmith, C. Little, N. Mangold, G. Manhes, P. Mauchien, C. McKay, E. Miller, J. Mooney, R. V. Morris, L. Morrison, T. Nelson, H. Newsom, A. Ollila, M. Ott, L. Pares, R. Perez, F. Poitrasson, C. Provost, J. W. Reiter, T. Roberts, F. Romero, V. Sautter, S. Salazar, J. J. Simmonds, R. Stiglich, S. Storms, N. Striebig, J.-J. Thocaven, T. Trujillo, M. Ulibarri, D. Vaniman, N. Warner, R. Waterbury, R. Whitaker, J. Witt, B. Wong-Swanson. The ChemCam Instrument Suite on the Mars Science Laboratory (MSL) Rover: Body Unit and Combined System Tests. *Space Sci. Rev.* **2012**. DOI: 10.1007/s11214-012-9902-4

[17] E. M. Galimov. Phobos sample return mission: scientific substantiation. *Sol. Sys. Res.* **2010**, 44, 5–14.

[18] L. M. Zelenyi, A. V. Zakharov. Phobos-Grunt project: devices for scientific studies. *Sol. Sys. Res.* **2010**, 44, 359–361.

[19] M. Y. Marov, V. S. Avduevsky, E. L. Akim, T. M. Eneev, R. S. Kremnev, S. D. Kulikov, K. M. Pickhadze, G. A. Popov, G. N. Rogovsky. Phobos-Grunt: Russian sample return mission. *Adv. Space Res.* **2004**, 33, 2276–2280.

[20] A. K. Knight, N. L. Scherbarth, D. A. Cremers, M. J. Ferris. Characterization of laser-induced breakdown spectroscopy (LIBS) for application to space exploration. *Appl. Spectrosc.* **2000**, 54, 331–340.

[21] W. B. Lee, J. Y. Wu, Y. I. Lee, J. Sneddon. Recent applications of laser-induced breakdown spectroscopy: A review of material approaches. *Appl. Spectrosc. Rev.* **2004**, 39, 27–97.

[22] J. Sneddon, Y. I. Lee. Novel and recent applications of elemental determination by laser-induced breakdown spectrometry. *Anal. Lett.* **1999**, 32, 2143–2162.

[23] K. Song, Y. I. Lee, J. Sneddon. Applications of laser-induced breakdown spectrometry. *Appl. Spectrosc. Rev.* **1997**, 32, 183–235.

[24] K. Song, Y. I. Lee, J. Sneddon. Recent developments in instrumentation for laser induced breakdown spectroscopy. *Appl. Spectrosc. Rev.* **2002**, 37, 89–117.

[25] P. Fichet, M. Tabarant, B. Salle, C. Gautier. Comparisons between LIBS and ICP/OES. *Anal. Bioanal. Chem.* **2006**, 385, 338–344.

[26] F. J. Fortes, J. J. Laserna. The development of fieldable laser-induced breakdown spectrometer: No limits on the horizon. *Spectrochimica Acta Part B* **2010**, 65, 975–990.

[27] R. Huang, Q. Yu, L. Li, Y. Lin, W. Hang, J. He, B. Huang. High irradiance laser ionization orthogonal time-of-flight mass spectrometry: a versatile tool for solid analysis. *Mass Spectrom. Rev.* **2011**, 30, 1256–1268.

[28] L. Li, B. Zhang, R. Huang, W. Hang, J. He, B. Huang. Laser ionization orthogonal time-of-flight mass spectrometry for simultaneous determination of nonmentallic elements in solids. *Anal. Chem.* **2010**, 82, 1949–1953.

[29] H. X. Sun, S. W. Dai, J. F. Yang, J. Wu, J. S. Jiang. Scientific objectives and payloads of Chang'E-1 lunar satellite. *J. Earth Syst. Sci.* **2005**, 114, 789–794.

[30] R. Huang, B. Zhang, D. Zou, W. Hang, J. He, B. Huang. Elemental imaging via laser ionization orthogonal time-of-flight mass spectrometry. *Anal. Chem.* **2011**, 83, 1102–1107.

[31] Q. Yu, L. Chen, R. Huang, W. Hang, J. He, B. Huang. Laser ionization time-of-flight mass spectrometry for direct elemental analysis. *Trends Anal. Chem.* **2009**, 28, 1174–1185.

[32] Q. Yu, R. Huang, L. Li, L. Lin, W. Hang, J. He, B. Huang. Applicability of standardless semiquantitative analysis of solids by high-irradiance laser ionization orthogonal time-of-flight mass spectrometry. *Anal. Chem.* **2009**, 81, 4343–4348.

[33] Q. Yu, Z. Cao, L. Li, B. Yan, W. Hang, J. He, B. Huang. Femtogram detection and quantization of residues using laser ionization orthogonal time-of-flight mass spectrometry. *Anal. Chem.* **2009**, *81*, 8623–8626.

[34] P. Wurz, D. Abplanalp, M. Tulej, M. Iakovleva, V. A. Fernandes, A. Chumikov, G. Managadze. Mass Spectrometric Analysis in Planetary Science: Investigation of the Surface and the Atmosphere. *Sol. Sys. Res.* **2012**, in press.

[35] P. Wurz, K. R. Lykke, M. J. Pellin, D. M. Gruen, D. H. Parker. Characterization of Fullerenes by Laser-Based Mass Spectrometry. *Vacuum* **1992**, *43*, 381–385.

[36] A. Bieler, K. Altwegg, L. Hofer, A. Jäckel, A. Riedo, T. Sémon, P. Wahlström, P. Wurz. Optimization of mass spectrometers using the adaptive particle swarm algorithm. *J. Mass Spect.* **2011**, *45*, 1143–1151.

[37] A. Bieler. Design of a novel time of flight mass spectrometer and practical application of computer optimization to the development and tuning of mass spectrometers. PhD Thesis, University of Bern, Switzerland, **2012**.

[38] Z.-H. Zhan, J. Zhang, Y. Li, H. S.-H. Chung. Adaptive particle swarm optimization. *IEEE Trans. Syst. Man Cybern. B Cybern.* **2009**, *39*(6), 1362–1381.

[39] J. Kennedy, R. Eberhart. Particle swarm optimization. *Proceedings of IEEE International Conference on Neural Networks* **1995**, *IV*, 1942–1948.

[40] Y. Shi, R. Eberhart. A modified particle swarm optmizer. *Proceedings of IEEE International Conference on Evolutionary Computation* **1998**, 69–73.

[41] T. Beck, A. Bieler, N. Thomas. Numerical thermal mathematical model correlation to thermal balance test using adaptive particle swarm optimization (APSO). *Appl. Therm. Eng.* **2012**, *38*, 168–174.

[42] G. G. Managadze, P. Wurz, R. Z. Sagdeev, A. E. Chumikov, M. Tulej, M. Iakovleva, N. G. Managadze, A. L. Bondarenko. Study of the Main Geochemical Charcteristics of Phobos' Regolith Using Laser Time of Fligght Mass Spectrometry. *EPSC Abstracts* **2011**, *6*, EPSC-DPS2011-1065.

[43] Concept Research Corporation. http://www.conceptsresearch.com, **2012**.

[44] J. Jost. Ansteuerung eines Lasers für ein Massenspektrometer einer ESA'Lander'-Mission. Diplom Thesis, University of Bern, Switzerland, **2002**.

[45] A. Balogh, M. Bird, L. Blomberg, P. Bochsler, J.-L. Bougeret, J. Brückner, L. Iess, J. Guest, Y. Langevin, A. Milani, J.-A. Sauvaud, W. Schmidt, T. Spohn, R. von Steiger, N. Thomas, K. Torkar, H. Wänke, P. Wurz. BepiColombo - An interdisciplinary cornerstone mission to the planet Mercury. *ESA-SCI(2000)1, Noordwijk, The Netherlands, European Space Agency*, **2000**.

[46] P. R. Mahaffy, C. R. Webster, M. Cabane, P. G. Conrad, P. Coll, S. K. Atreya, R. Arvey, M. Barciniak, M. Benna, L. Bleacher, W. B. Brinckerhoff, J. L. Eigenbrode, D. Carignan, M. Cascia, R. A. Chalmers, J. P. Dworkin, T. Errigo, P. Everson, H. Franz, R. Farley, S. Feng, G. Frazier, C. Freissinet, D. P. Glavin, D. N. Harpold, D. Hawk, V. Holmes, C. S. Johnson, A. Jones, P. Jordan, J. Kellogg, J. Lewis, E. Lyness, C. A. Malespin, D. K. Martin, J. Maurer, A. C. McAdam, D. McLennan, T. J. Nolan, M. Noriega, A. A. Pavlov, B. Prats, E. Raaen, O. Sheinman, D. Sheppard, J. Smith, J. C. Stern, F. Tan, M. Trainer, D. W. Ming, R. V. Morris, J. Jones, C. Gundersen, A. Steele, J. Wray, O. Botta, L. A. Leshin, T. Owen, S. Battel, B. M. Jakosky, H. Manning, S. Squyres, R. Navarro-González, C. P. McKay, F. Raulin, R. Sternberg, A. Buch, P. Sorensen, R. Kline-Schoder, D. Coscia, C. Szopa, S. Teinturier, C. Baffes, J. Feldman, G. Flesch, S. Forouhar, R. Garcia, D. Keymeulen, S. Woodward, B. P. Block, K. Arnett, R. Miller, C. Edmonson, S. Gorevan, E. Mumm. The sample Analysis at Mars Investigation and Instrument suite. *Space Sci. Rev.* **2012**, 1–78.

[47] S. Scherer, K. Altwegg, H. Balsiger, J. Fischer, A. Jäckel, A. Korth, M. Mildner, D. Piazza, H. Rème, P. Wurz. A novel principle for an ion mirror design in time-of-flight mass spectrometry. *Int. J. Mass Spectr.* **2006**, *251*, 73–81.

[48] Creare Inc., Hanover, New Hampshire, http://www.creare.com, **2012**.

[49] P. Wurz, D. Aplanalp, M. Tulej, H. Lammer. A neutral gas mass spectrometer for the investigation of lunar volatiles. *Planet. Sp. Sci.* **2012**, in press, DOI: 10.1016/j.pss.2012.05.016

[50] J. S. Becker. *Inorganic Mass Spectrometry, Principles and Applications*. John Wiley & Sons Ltd: England, **2007**.

[51] A. Riedo, S. Meyer, B. Heredia, M. Neuland, A. Bieler, M. Tulej, M. Iakovleva, K. Mezger, P. Wurz. Highly accurate isotope composition measurements by a miniature laser ablation mass spectrometer designed for in situ investigations on planetary surfaces. *PSS* **2012**, submitted.